RESEARCH

Energy evolution and water immersion-induced weakening in sandstone roof of coal mines

Wenjie Liu[1,3,4] · Ke Yang[1,2,3,4] · Shuai Zhang[5] · Zhainan Zhang[1,3,4] · Rijie Xu[1,3,4]

Abstract

The instability of underground spaces in abandoned coal mines with water-immersed rocks is one of the main hazards hindering the geothermal energy use and ecological restoration of post-mining areas. This study conducted graded cyclic loading–unloading tests of five groups of sandstone samples with different water contents. The evolution of input, elastic, dissipated, damping, and plastic energies were explored, considering the damping effect. The normalized plastic energy serves to characterize the damage evolution of sandstone samples, whose failure characteristics were analyzed from both the macroscopic and microscopic perspectives. X-ray diffraction technique and scanning electron microscopy were used to reveal the softening mechanism of sandstone. The results show that under graded cyclic loading, input energy, elastic energy, and dissipated energy all increase gradually, and the fraction of elastic energy increases gradually at first and then tends to stabilize. The variation in the fraction of dissipated energy is opposite to that of elastic energy. In each cycle, the input energy is stored primarily in the form of elastic energy, whereas the dissipated energy is used primarily to overcome the damping of sandstone. When the normalized number of cycles approached unity, the plastic energy fraction sharply increases, while that of the dampening energy drops abruptly. With increasing water content, the effect of pore water on the lubrication, the water wedge, and dissolution of mineral particles becomes more obvious, reducing the elastic-storage limit of sandstone, meanwhile the sandstone damage factor increases significantly under the same cycle and the failure mode changes from brittle to ductile.

Keywords Mining engineering · Energy evolution · Water–rock interaction · Weakening mechanism

1 Introduction

After the closure of coal mines due to low economic benefit or resource exhaustion, the surface water and groundwater contained in the aquifer rapidly fill underground spaces through the fissured zone, causing a drop in groundwater level, water pollution, surface subsidence, changes in the geological environment, and secondary disasters (Li et al. 2019; Sun et al. 2021). Within the framework of clean-energy production and ecological restoration of the post-mining areas, considerable efforts have been made worldwide to use geothermal energy, water, and spaces in abandoned coal mines. For example, some scholars have suggested constructing underground reservoirs from abandoned coal mines (Bian et al. 2021; Gu et al. 2015), developing geothermal resources (Pu et al. 2021; Jardon et al. 2013), or building pumped storage power stations (Fan et al. 2020; Xie et al. 2020).

✉ Ke Yang
  keyang2003@163.com

1   State Key Laboratory of Mining Response and Disaster Prevention and Control in Deep Coal Mines, Anhui University of Science and Technology, Huainan 232001, China

2   Hefei Comprehensive National Science Center, Institute of Energy, Hefei 230031, Anhui, China

3   National and Local Joint Engineering Research Center of Precision Coal Mining, Anhui University of Science and Technology, Huainan 232001, Anhui, China

4   Key Laboratory of Mining Coal Safety and Efficiently Constructed By Anhui Province and Ministry of Education, Anhui University of Science and Technology, Huainan 232001, China

5   State Key Laboratory of Coal Resources and Safe Mining, China University of Mining and Technology, Xuzhou 221116, Jiangsu, China

Complex water–rock interactions, physical effects, and chemical reactions commonly occur in abandoned coal mines due to tidal action and water erosion, significantly deteriorating rock stability and residual strength. This issue was addressed by numerous scholars, who investigated the mechanical characteristics and failure mechanism of water-bearing rocks (Wong et al. 2016; Hashiba et al. 2015; Guo et al. 2021) and conducted post-peak cyclic loading–unloading tests for coarse sandstone in natural and water-saturated conditions (Niu et al. 2018). The latter found that the water-saturated coarse sandstone exhibited a more significant increase in lateral and volumetric strains compared with the natural condition. In uniaxial loading–unloading tests, water saturation had an apparent softening effect on post-peak fractured coarse sandstone strength and elastic modulus. Zhou et al. (2016) conducted static and dynamic mechanical tests of sandstone samples with different water contents under the dry–wet cycles. They found that water-bearing sandstone could gradually restore its mechanical characteristics in dry conditions. The tensile strength of drying versus water-immersed sandstone with the same water content differs. Hua et al. (2019) compared the mechanical fracture characteristics of sandstone under dry–wet cycling and long-term water immersion and reported that dry–wet cycling causes more significant deterioration due to sandstone fracture than long-term water immersion. Rock damage and failure are closely related to energy accumulation, dissipation, and release. Therefore, some scholars have analyzed how water affects rocks from an energy perspective (Li et al. 2015; Wang et al. 2017). Chen et al. (2019) pointed out that the amount of energy released upon sandstone compaction and elastic deformation stages increases significantly. The water content increases and the amount of energy released after failure decreases. A higher water content leads to a reduction of sandstone brittleness and enhances its plastic deformation. Geng et al. (2020) conducted uniaxial compression tests on dry, water-bearing, and saturated sandstone samples. Their results show that the water-softened sandstone is more prone to ductile damage and releases less elastic energy. Ma et al. (2018) carried out uniaxial compression testing of gypsum rocks under different durations of water immersion, and the results show that the input, elastic, and dissipated energies of gypsum rock decrease with increasing water-immersion time. Using a constitutive damage model based on energy dissipation, they further described the damage characteristics of gypsum rock weakened by water and under a uniaxial load.

As discussed above, the mechanical characteristics, energy evolution, and failure modes of water-bearing sandstone during deformation and failure processes have been extensively studied. However, studies are scarce on the evolution of residual plastic strain in sandstone with different water content and graded cyclic loading. In addition, few works consider the hysteresis effect of rocks and the energy dissipated by damping. The present study thus considers uniaxial loading and cyclic loading–unloading tests of sandstone samples with different water contents and determines the mechanical response of sandstone samples with different water contents under graded cyclic loading–unloading. Considering the viscoelastic properties of sandstone, we determine how damping and dissipated energy evolve. How sandstone damage evolves during the deformation and failure is also quantitatively described based on the energy principle. Macroscopic crack propagation within sandstone samples was monitored using digital speckle technology. Scanning electron microscopy (SEM) was used to image the microstructure of fractured sandstone samples. Finally, the mechanism by which water immersion weakens the mechanical properties of the sandstone is revealed. These research findings offer theoretical support for evaluating the safety and stability of rocks in coal mine underground reservoirs.

2 Energy conversion theory considering viscoelastic deformation

Under cyclic loading, the entire process of sandstone deformation and failure is accompanied by energy accumulation, release, and dissipation. To use the first law of thermodynamics, we assume that the sandstone does not exchange thermally with the environment during deformation and failure, and we neglect any radiant energy and acoustic-emission energy. The work done by the press machine on the sandstone samples is the total input energy. As shown in Fig. 1 and according to Xie et al. (2005), the energy accumulated in each cycle can be calculated by Eqs. (1)–(4):
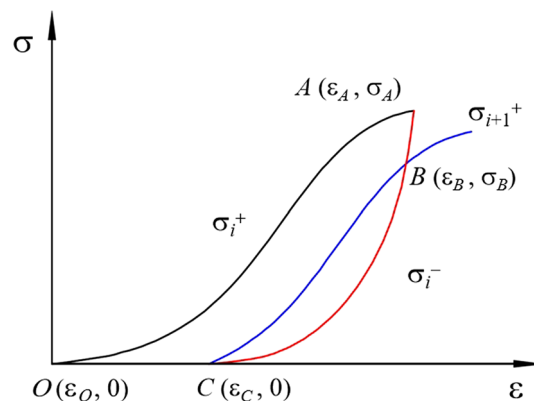
$$U_i = U_{ei} + U_{dis i}, \tag{1}$$

Fig. 1 Stress path of cyclic loading–unloading

$$U_i = \int_{\varepsilon_o}^{\varepsilon_A} \sigma_i^+ \, d\varepsilon_i, \tag{2}$$

$$U_{ei} = \int_{\varepsilon_c}^{\varepsilon_A} \sigma_i^- \, d\varepsilon_i, \tag{3}$$

$$U_{disi} = U_i - U_{ei} = \int_{\varepsilon_o}^{\varepsilon_A} \sigma_i^+ \, d\varepsilon_i - \int_{\varepsilon_c}^{\varepsilon_A} \sigma_i^- \, d\varepsilon_i, \tag{4}$$

where U_i, U_{ei}, and U_{disi} are the input, elastic, and dissipated energies of cycle i, respectively, σ_i^+ and σ_{i+1}^+ are the stresses imposed on loading i and $i+1$, respectively, and σ_i^- is the stress imposed upon unloading i.

Rocks are aggregates of mineral particles with complex mineral composition and structure, which gives them their significant heterogeneity and anisotropy. In most studies on energy evolution in rocks under graded cyclic loading and unloading, rocks are treated as elastoplastic materials. The area enclosed by the cyclic loading–unloading curve and the coordinate axis (U_{disi}) is treated as the energy that causes rock damage and failure. However, such an assumption neglects the viscous friction between mineral particles and the liquid. Therefore, the plastic energy causing rock damage is not differentiated from the damping energy spent on overcoming the viscous friction. In the present study, we consider the viscoelastic deformation of sand-bearing sandstone. For each cyclic loading, the dissipated energy U_{disi} is split into plastic energy U_{pi} and damping energy U_{dami}. We assume that damping does not cause sandstone damage and failure, and the plastic energy promotes the plastic deformation of rocks, which weakens the sandstone.

The stress path of a single loading–unloading cycle is analyzed separately, as shown in Fig. 1, where point O is the starting point of cyclic-loading curve i, point A is the end point of cyclic-loading curve i and the starting point of cyclic-unloading curve i, point B is the intersection between cyclic-unloading curve i and cyclic-loading curve $i+1$, point C is the end point of cyclic-unloading curve i and the start point of cyclic-loading curve $i+1$, ε_o, ε_A, ε_B, and ε_C are the strain at the corresponding coordinates, respectively, and σ_A and σ_B are the stress at the corresponding coordinates, respectively. The cyclic elastic strain ε_{ei} for cycle i is defined as the difference between the peak strain ε_A of cycle i and the residual plastic strain ε_C of cycle i, the residual plastic strain ε_{pi} is the difference between the strain ε_o at the starting point of the loading curve of cycle i (point O) and the strain ε_C at the endpoint of the unloading curve of cycle i.

As shown in Fig. 1, the physical meaning of point B is approximately the stress state during loading–unloading cycle i. Unloading starts from this stress state, followed by another loading. Then, the sandstone returns to the initial stress state, thus forming the closed hysteresis loop BCB.

For a rock treated as an elastoplastic material, the shape of the hysteresis loop under elastoplastic deformation is jointly determined by rock viscosity and plasticity. Rock as an elastoplastic material undergoes no plastic deformation, and its unloading paths differ. Nevertheless, a closed hysteresis loop can still be formed for the rock. Stevens et al. (1980) and Kuwahara et al. (1990) found that, under a loading–unloading action, numerous microcracks appear in rocks only when the stress during the second loading exceeds the peak stress upon first loading. It was believed that, during uniaxial graded loading and unloading, no new cracks are generated in the rocks if the loading stress is less than the stress during the previous loading. In this case, there would be no growth in plastic energy. Based on this argumentation, we assume that sandstone is an elastoplastic material along the stress path from point B to point C upon unloading and back to point B upon loading. At this stage, the sandstone undergoes elastoplastic deformation, and the elastic energy is not dissipated. The energy lost during this cycle is the work done by damping that arose from rock viscosity.

Similarly, we assume that the sandstone does exchange thermally with the environment (thermal radiation and acoustic-emission energy are neglected). Thus, the area of the hysteresis loop BCB is the energy dissipated by overcoming the viscous friction between the mineral particles and liquid, i.e., the damping energy U_{dami}. The dissipated energy U_{di} minus this portion of the damping energy is the plastic energy U_{pi} that causes rock damage. The relationship between these energies and their magnitude can be calculated using Eqs. (5)–(7):

$$U_{disi} = U_{pi} + U_{dami}, \tag{5}$$

$$U_{dami} = \int_{\varepsilon_o}^{\varepsilon_B} (\sigma_{i+1}^+ - \sigma_i^+) \, d\varepsilon_i, \tag{6}$$

$$U_{pi} = \int_{\varepsilon_o}^{\varepsilon_A} \sigma_i^+ \, d\varepsilon_i - \int_{\varepsilon_C}^{\varepsilon_A} \sigma_i^- \, d\varepsilon_i - \int_{\varepsilon_o}^{\varepsilon_B} (\sigma_{i+1}^+ - \sigma_i^+) \, d\varepsilon_i. \tag{7}$$

3 Experimental setup and test scheme

3.1 Sample preparation

The sandstone samples were collected from the No. 4 coal seam roof of the Panbei Coal Mine in Huainan and Huaibei Mining Area, China. Unweathered sandstone samples with good integrity and uniform texture were sealed in wax at the collection site and transported to the laboratory. According to the requirements of the International Society for Rock Mechanics and Rock Engineering, the sandstone was cut,

drilled, and polished into standard cylindrical samples with a diameter of 50 mm and length of 100 mm. Thirty standard samples were subdivided into five groups and prepared for testing. Before the mechanical tests, the sandstone samples were dried at 105 ℃ in an oven for 24 h until attaining a constant weight. Next, samples of each group were removed and placed into distilled water for natural water-immersion tests (Yu et al. 2019). Each sandstone sample was weighed before and after each experimental step. According to Eq. (8), the native water content of the sandstone samples was calculated to be approximately 0.3%, and the water content of the water-saturated sandstone sample was about 2.07%. The water content is given by

$$W = \{(M_w - M_0)/M_0\} \times 100\% \qquad (8)$$

where W is water content in percent, and M_w and M_0 are the mass of wet and dry sandstone samples, respectively.

Sandstone quality was measured every 2 h during natural water-immersion tests, and Fig. 1 shows the water-absorption curve of the sandstone samples over the whole process (500 h). When water-absorption exceeded 200 h, the water-absorption quality of the sandstone sample remained essentially constant, so we considered that the sandstone had reached its saturation state. At this point, the mass of the water-absorbed sample was 10.83 g (Fig. 2).

As shown in Fig. 3, sandstone samples with five levels of water content were prepared: 0%, 0.50%, 1.01%, 1.52%, and 2.07%. Uniaxial compression and uniaxial graded cyclic loading–unloading tests were done on the sandstone samples. Six samples were used at each level of water content. To avoid data contingency, three of them were used for uniaxial tests, and the other three were used for graded cyclic loading and unloading tests. After the experiment, valid data
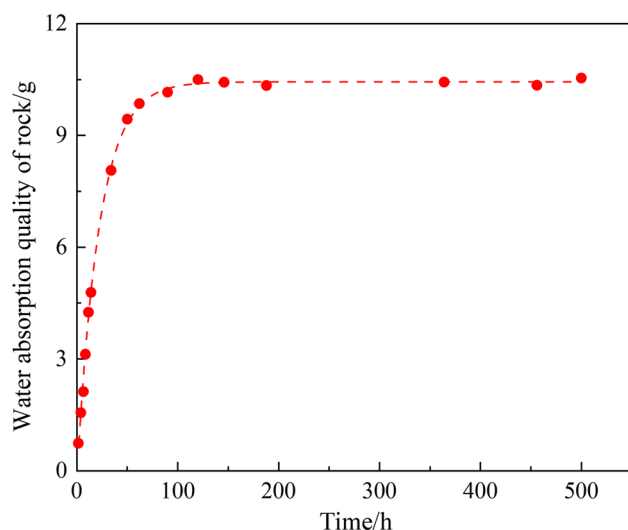

Fig. 2 Spontaneous imbibition curve of sandstone samples

Fig. 3 Sandstone samples with different water contents

were selected from each group for analysis. Given that environmental factors affect the experimental results, the tests were done immediately after the preparation of each group of samples.

3.2 Test system

As shown in Fig. 4, the test system mainly consisted of a rock mechanical testing module, a digital video acquisition module, an SEM testing module, and an x-ray diffraction (XRD) testing module. The rock mechanical testing module consisted of an RMT-150B multifunction automatic rigid rock servo material testing machine, which was used for high-precision uniaxial and triaxial compression tests. The maximal axial load imposed by this machine was 1000 kN, with a loading rate of 0.01–100 kN/s. The measuring range of the axial displacement sensor was 0–5 mm, with a resolution of 0.0015 m, which satisfied the test requirements. The SEM testing module consisted of a FLEXSEM 1000, a compact SEM, for high-resolution imaging in low-vacuum mode. The magnification factor ranged from 60,000 to 300,000, with an accelerating voltage of 0.3–20 kV and a resolution of 4 nm. The XRD testing module consisted of a SmartLab X-ray diffractometer for analyzing the mineral composition of the sandstone samples. The digital video acquisition module consisted of a Nikon digital camera, which served to capture the fracture morphology of the sandstone samples during the loading process.

3.3 Experimental scheme and results

Each group of the sandstone samples was further split into subgroups U and C, which were used for the uniaxial compression and uniaxial graded loading–unloading tests, respectively. To improve the experimental accuracy and reduce the randomness of the experimental results, no less than three parallel tests were conducted for each loading scheme and for each water content. The uniaxial compression tests were first conducted to obtain the strain–stress
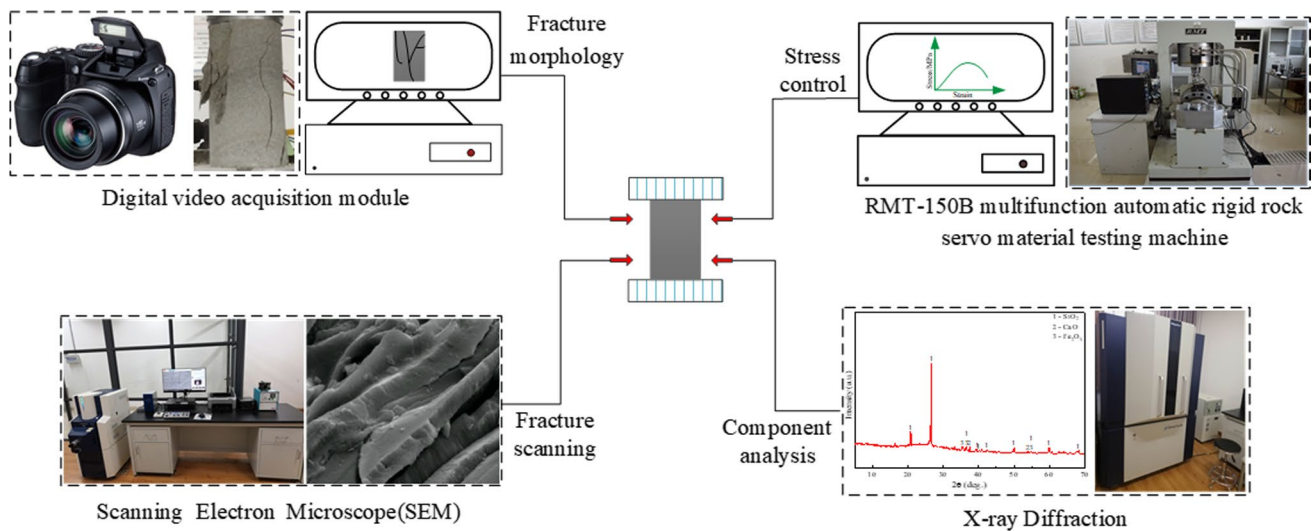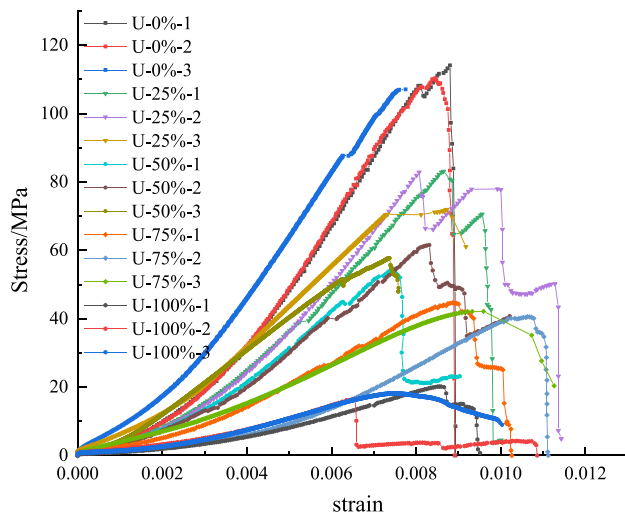
Fig. 4 Test system

Fig. 5 Stress–strain curve under uniaxial loading

Fig. 6 Stress path of the cyclic loading–unloading test

curves for different water contents, as shown in Fig. 5. Next, the axial pressure at each unloading point was determined to design the subsequent cyclic loading–unloading test. The stress-controlled mode was implemented in the uniaxial cyclic loading–unloading tests, as shown in Fig. 6.

The loading and unloading rates were both 0.5 MPa/s. The stress gradient during the loading stage was 5 MPa. The target stress of unloading for the unloading stage was set to 1.25 MPa. The stress path of the uniaxial cyclic loading–unloading test was 0, 5, 1.25, 10, 1.25, 15, 1.25, 20, 1.25, 25, 1.25, 30 MPa, sample failure, test termination. To facilitate the analysis of the test results, we normalized the water content. The saturated water content was defined as 100%. Next, the samples in each group were numbered.
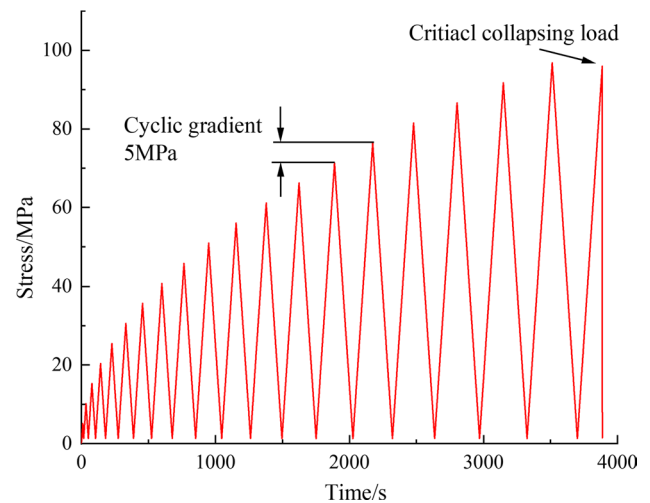
For example, C-25%-1 refers to the uniaxial graded cyclic loading–unloading test for the first group of samples with a water content of 0.50%, and U-75%-3 refers to the uniaxial compression testing of the third group of samples with a water content of 1.52%.

Figure 7 shows the XRD results for the mineral composition of the three groups of sandstone samples with different water contents. The sandstone samples were composed of mineral crystals, including quartz, kaolinite, albite, and calcite. The quartz content was the highest of all the minerals in the three groups of samples, accounting for about 50% by mass. The sandstone samples with different water contents varied in mineral composition and content. The sandstone samples with zero water content contained mainly two
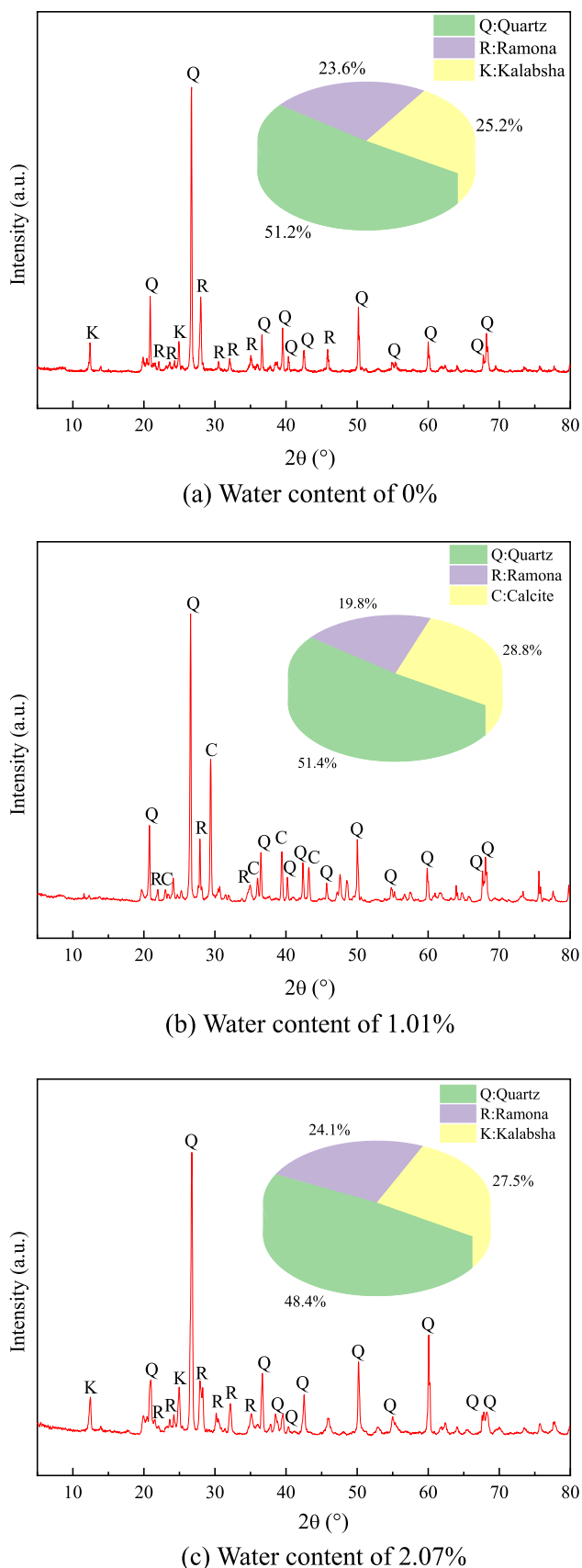
(a) Water content of 0%

(b) Water content of 1.01%

(c) Water content of 2.07%

Fig. 7 XRD patterns of sandstone samples

minerals, whereas those with a water content of 2.07% contained mainly three minerals. Variations in mineral content did not correlate significantly with water content.

4 Analysis of mechanical characteristics of sandstone samples under cyclic loading

The softening coefficient was used to more intuitively characterize the softening properties of sandstone samples with different water contents. The softening coefficient λ is defined as the ratio of the compressive strength R_w of the water-bearing sandstone samples with different water contents to the compressive strength R_d of the dry sandstone:

$$\lambda = \frac{R_w}{R_d}, \quad 0 < \lambda \le 1. \tag{9}$$

The smaller the softening coefficient, the stronger the softening and the greater the impact of water on the rocks. As shown in Table 1, water significantly affects the mechanical properties of sandstone. Compared with dry samples, the average uniaxial compressive strength of water-bearing sandstone significantly dropped with water content from the initial 110.51 to 18.23 MPa. The average elastic modulus of the sandstone also decreased continuously from 19.61 to 3.53 GPa as the water content increased. Conversely, Poisson's ratio increased.

Figure 8 shows the stress–strain curves of different groups of sandstone samples subjected to graded cyclic loading–unloading tests. All sandstone samples underwent recoverable plastic deformation during each loading–unloading cycle and unrecoverable plastic deformation. Before failure, the stress–strain curve deviates from the historical stress–strain curve. In addition, as the irreversible plastic deformation accumulates, the cyclic loading–unloading curve gradually shifts toward larger strain. Under graded cyclic loading–unloading, the sandstone strength and the number of loading–unloading cycles before failure gradually decrease as the water content increases.

For the sake of convenience, we normalized the number of cycles before failure. Figure 9 shows the curves of elastic strain ε_{ei} or residual plastic strain ε_{pi} versus the normalized number of cycles. These results show that the sandstone undergoes plastic strain and residual plastic strain in each cycle. Since the rock is an inhomogeneous anisotropic material, the primary pores and cracks within the sandstone are gradually compacted under initial cyclic loading. At this stage, the elastic strain curve versus the normalized number of cycles increases nonlinearly, and the residual plastic strain is larger than the other stage. The sandstone enters the plastic deformation stage in the subsequent cycles as the number of cycles and stress increase. The elastic strain increases

Table 1 Mechanical parameters under different water contents

Sample	Water content (%)	Uniaxial compressive strength (MPa)	Elastic modulus (GPa)	Poisson's ratio	Average softening coefficient
U-0%-1	0.00	114.09	19.70	0.11	1
U-0%-2	0.00	110.35	20.36	0.11	
U-0%-3	0.00	107.09	18.79	0.12	
U-25%-1	0.50	83.12	13.91	0.16	0.72
U-25%-2	0.53	82.89	15.41	0.14	
U-25%-3	0.48	71.93	12.43	0.17	
U-50%-1	1.01	61.52	10.58	0.21	0.52
U-50%-2	1.04	54.60	10.84	0.19	
U-50%-3	1.02	57.70	9.27	0.22	
U-75%-1	1.52	44.47	6.21	0.26	0.38
U-75%-2	1.49	40.56	6.65	0.24	
U-75%-3	1.53	42.12	5.84	0.24	
U-100%-1	2.07	16.39	3.47	0.31	0.16
U-100%-2	2.03	20.14	3.67	0.32	
U-100%-3	2.08	18.17	3.45	0.29	

(a) Water content of 0%   (b) Water content of 0.50%   (c) Water content of 1.01%

(d) Water content of 1.52%   (e) Water content of 2.07%
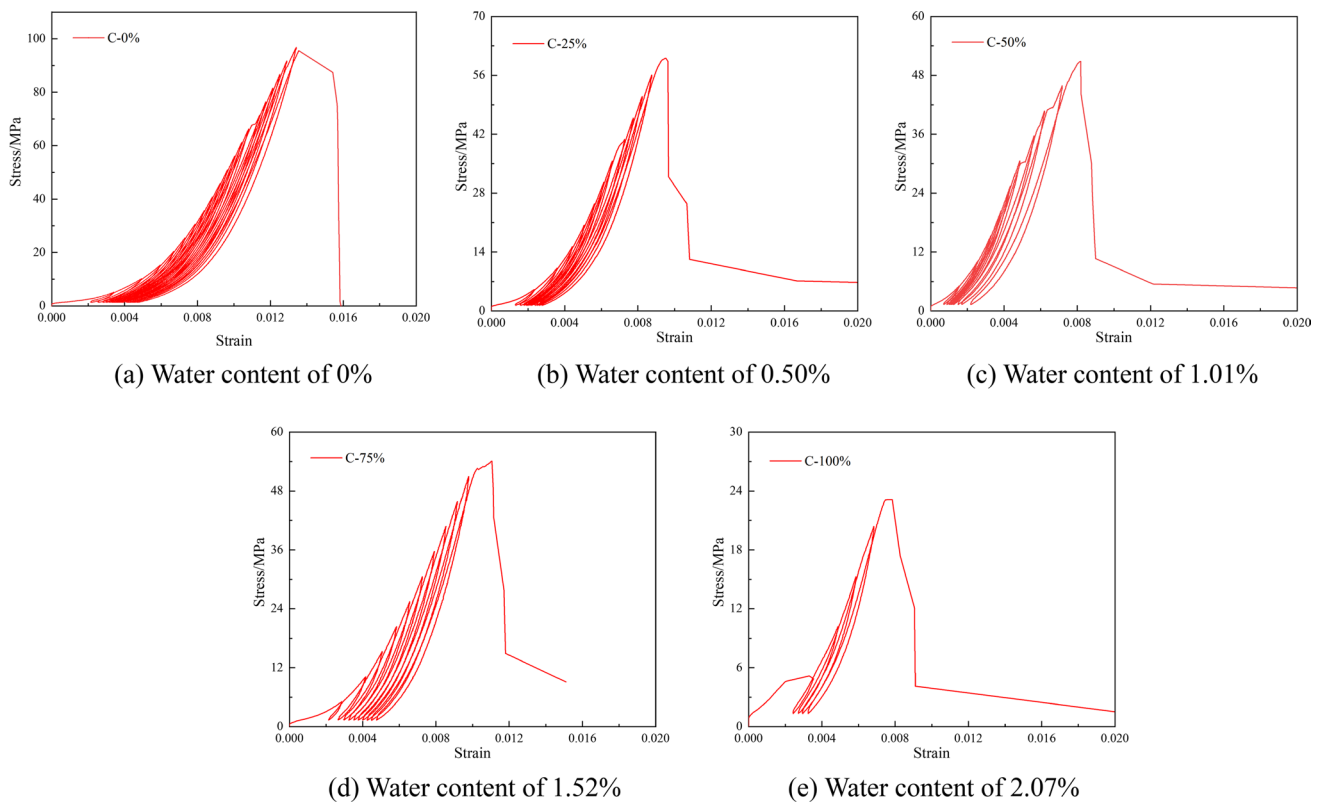
Fig. 8 Cyclic stress–strain curves

approximately linearly versus the normalized number of cycles. At this stage, the residual plastic strain decreases rapidly and stabilizes. When the residual strain accumulates to a certain level, microcracks within the sandstone become interconnected and penetrate the samples. The residual plastic strain increases slightly versus the normalized number of cycles. For the same number of normalized cycles, the elastic strain of sandstone decreases gradually with increasing
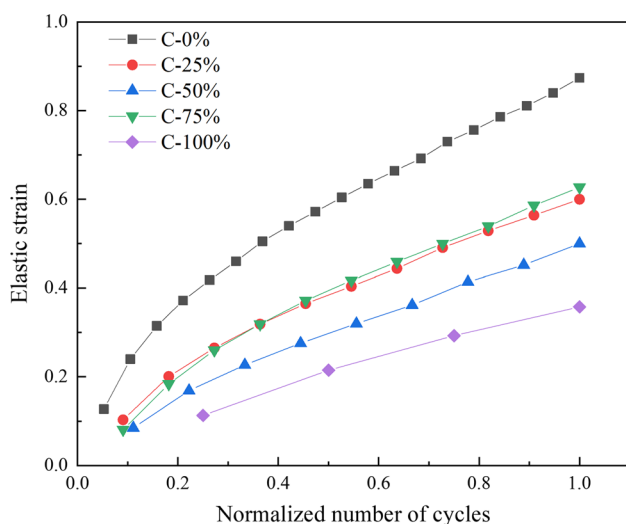
(a) Elastic strain
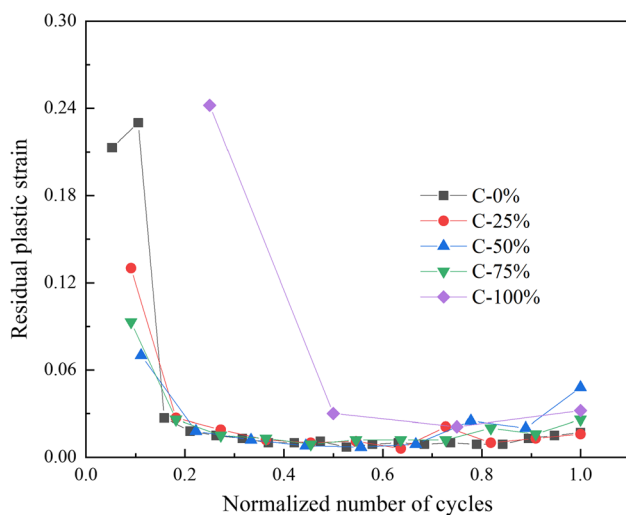
(b) Plastic strain

Fig. 9 Elastic strain and plastic strain curves

water content. With a saturated water content, the residual plastic strain increases significantly, which shows that with the increase of water content, the degree of plastic damage of sandstone under the same external load gradually increases.

5 Energy evolution analysis

5.1 Energy evolution law

According to theoretical background and Eqs. (1)–(4) in Sect. 2, we derived the evolution of the elastic and dissipated energies and plot their fraction in sandstone samples

as a function of water content. The results in Fig. 10 lead to the following observations:

(1) The input, elastic, and dissipated energies of sandstone samples with different water contents increase with the normalized number of cycles because a greater number of cycles implies more work done on the sandstone sample by the external force. As a result, the input energy increases. Part of the input energy is stored in the sandstone in the form of elastic energy, and the remaining part is dissipated via rock damage.

(2) Comparing the shares of elastic energy and dissipated energy as a function of water content shows that, under the initial cyclic loading, the input energy mainly takes the form of dissipated energy, which significantly exceeds the share of elastic energy. Under initial loading, the sandstone is damaged and fails due to the compression of primary defects, leading to more significant energy dissipation. Besides, the larger the water content, the higher the dissipated energy share and the more severe the sandstone damage under initial loading.

(3) As the normalized number of cycles increases, the elastic energy gradually increases, and the dissipated energy decreases until finally stabilizing. These results indicate that, at this stage, the input energy is stored in the sandstone mainly in the form of elastic energy. The fraction of elastic energy ranges from 0.7 to 0.9. In addition, a greater water content leads to less elastic energy and more severe sample damage under the same stress.

(4) When the normalized number of cycles approaches unity, the input, elastic, and dissipated energies continue to increase. The elastic energy decreases, and the dissipated energy increases, which indicates that the microcracks within the sandstone gradually propagate and penetrate the sandstone sample, resulting in its failure. Given the above, we predicted the sandstone failure based on the energy evolution.

Using Eqs. (5)–(7), we calculate the evolution of the damping energy, plastic energy, and their shares in sandstone samples as a function of water content. The results appear in Fig. 11 and show that, with increasing cycle number, the damping energy and the plastic energy in the sandstone increase gradually for all water contents. The plastic energy first decreases rapidly, then stabilizes, and later increases abruptly. The damping energy follows the opposite trend. Such variations are considered relevant to rock compression and peak damage. The dissipated energy in the sandstone samples decreases with increasing water content. Most of the dissipated energy in each cycle is spent on overcoming the work done by viscosity. As the water content increases,
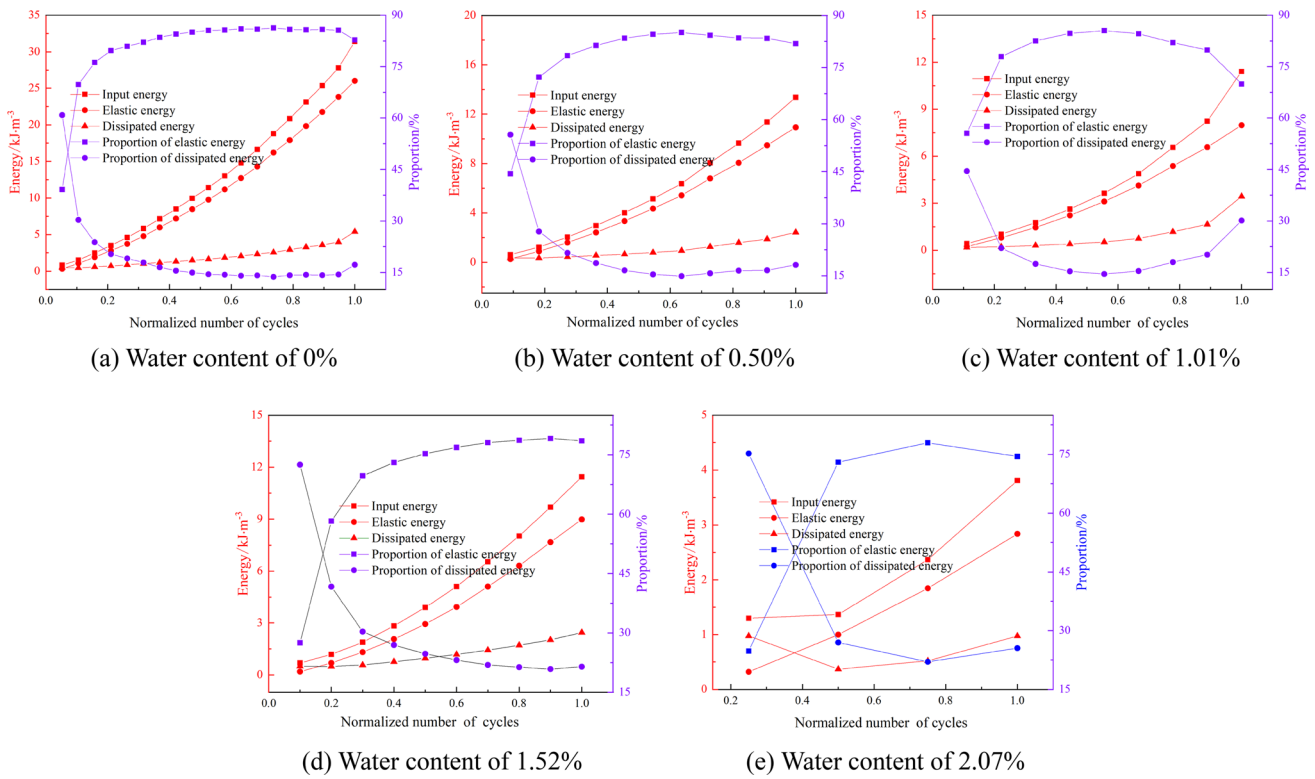
(a) Water content of 0%   (b) Water content of 0.50%   (c) Water content of 1.01%

(d) Water content of 1.52%   (e) Water content of 2.07%

Fig. 10 Energy distribution diagram

(a) Water content of 0%   (b) Water content of 0.50%   (c) Water content of 1.01%

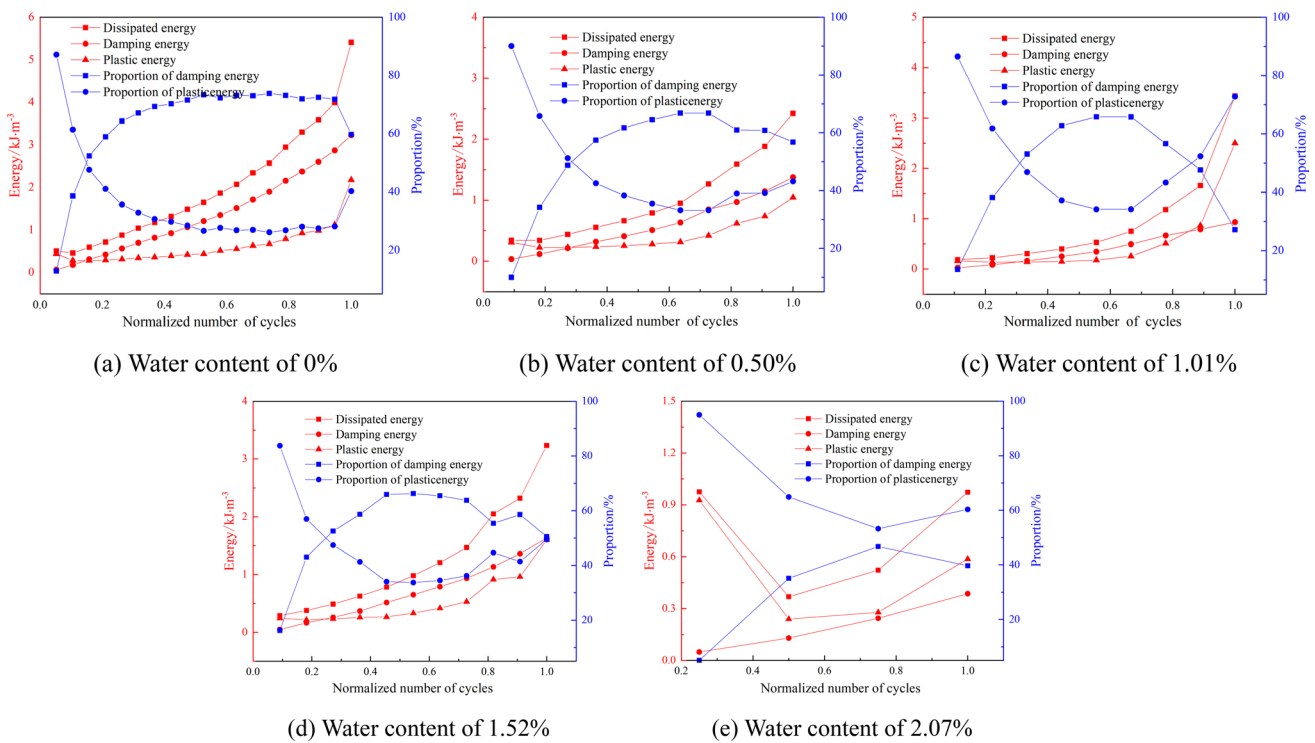(d) Water content of 1.52%   (e) Water content of 2.07%

Fig. 11 Dissipated energy distribution diagram

the plastic energy gradually overcomes the damping energy, which indicates that water immersion significantly reduces the work done by frictional damping between the mineral particles. As a result, the bonding strength between the mineral particles decreases, promoting sandstone damage and failure. The variation of the elastic energy share is like that of the dissipated energy. When the normalized number of cycles approaches unity, the plastic energy share increases abruptly. In contrast, the damping energy share drops sharply, portending the impending failure of the sandstone sample.

5.2 Damage mechanism based on plastic energy

Based on the results detailed above, the input energy under cyclic loading–unloading conditions was stored or released mainly in the form of elastic energy or dissipated in the form of damping energy. Only a small share of the input energy was spent on sandstone damage and failure. In addition, the higher the water content, the larger the plastic energy share under the same stress gradient. To characterize the degree of rock damage and failure, Liu et al. (2018) normalized the dissipated energy. They analyzed the cumulative damage of rocks under cyclic loading. Plastic energy was a primary factor causing rock damage, whereas damping energy did not lead to residual deformation or damage. Therefore, we considered it more accurate and reasonable to use normalized plastic energy to characterize rock damage. The damage factor D was defined as the ratio of cumulative damage to total damage:

$$D = \frac{\sum U_{pi}}{U_p}, \tag{10}$$

where U_{pi} is the plastic energy generated during cycle i, and U_p is the total plastic energy.

The damage variable estimated by this formula varies from zero to unity, satisfying the principle of damage irreversibility. Taking a dry sandstone sample (C-0) as an example, the damage factor evolution is plotted in Fig. 12 and may be subdivided into three stages: decelerating growth, stable growth, and accelerating growth.

At the stage of decelerating growth, the damage factor grows at a saturating rate under the initial cyclic loading due to rock anisotropy and heterogeneity. The damage factor reaches 35% at the stage of decelerating growth. At the stable growth stage, the damage generated per cycle gradually approaches a constant as the graded cyclic loading increases. This stage accounts for the majority of the loading–unloading cycles. These results indicate that damage accumulates stably, whereas microcracks initiate and propagate without coalescing and penetrating the samples' bulk. When the damage reaches about 80%, its accumulation accelerates.
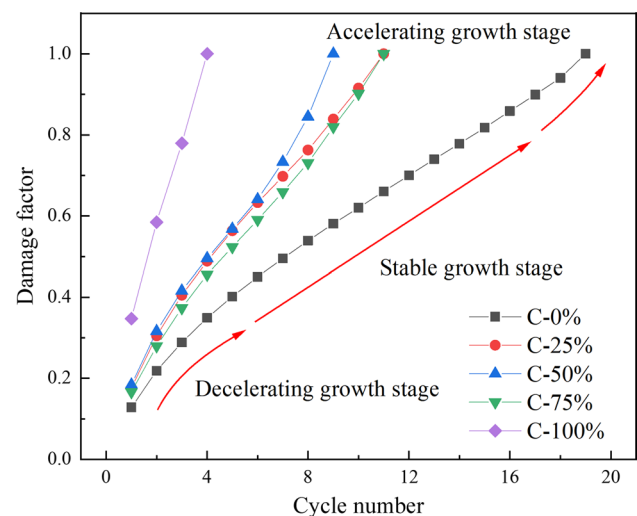
Fig. 12 Damage evolution curve

The damage generated in the previous two to three cycles accounts for nearly 24% of the total damage, resulting in instability and failure. These results indicate that, as the test proceeds, the pores and cracks propagate and become interconnected. After the cracks propagate to a certain degree, crack development and damage accumulation accelerate. As the water content increases, the curve of the damage factor as a function of cycle number shifts towards the y axis, and the region corresponding to the decelerating growth stage gradually disappears. This implies that under the graded cyclic loading conditions, a higher water content corresponds to faster growth of the damage factor. In the water-saturated sandstone sample (C-100), the damage generated in the first cycle accounts for about 34% of the total damage.

6 Fracture morphology and failure modes

Rock damage accumulation is the process whereby microcracks initiate, propagate, and become interconnected within the rocks. Fracture morphology characteristics vary at different stages of crack development. The fracture surface is where the microcracks and pores appear in large numbers. Microcracks and pores propagate along the weakest plane until the penetrating fracture surface is formed, leading to varying failure modes in the sandstone. We studied the microscopic fracture characteristics of cracks along with the macroscopic failure morphology of sandstone. Therefore, the impact of water on the sandstone failure process was investigated on both the microscopic and macroscopic scales. This approach was conducive to disclosing the macroscopic mechanism that weakens the mechanical strength and the energy-dissipation mechanism in water-bearing sandstone.

6.1 Fracture morphology

A Flex SEM1000 was used to image typical fractures in dry, semi-saturated, and saturated sandstone samples under graded cyclic loading–unloading. Figure 13 shows images of the microstructural variations in the sandstone samples at different magnifications. The images show that the fractures in the dry sandstone samples are serrated, the mineral particles form dense structures, and the cementing materials between the particles are compacted. Some micropores and cracks appear only along the mineral particle boundaries and in the cementing materials. In the semi-saturated sandstone samples, the microstructure patterns vary significantly. Corrosion pits appeared on the particle surfaces. Numerous secondary minerals and residues adhere to the mineral particle surfaces. In the saturated sandstone samples, significant dissolution and corrosion of the calcareous cement are apparent in loose structures. The cracks develop and propagate, and the mineral particles are more rounded. As analyzed above, the degree of cementation decreases in sandstone due to water immersion. The frictional damping between the particles weakens. Consequently, the sandstone samples gradually evolve from dense structures to lose structures. The water–rock interaction and the loading–unloading cycles promote damage accumulation and microstructural changes in sandstone samples.

6.2 Failure mode

With the development of monitoring technologies, digital imaging methods have become instrumental for studying macroscopic-crack propagation in rocks. The preparation of artificial speckles on the surface of the water-bearing sandstone samples increases the test duration. To mitigate this problem, we used the PhotoInfor and PostViewer image analysis software packages to determine sandstone deformation and failure during the tests (Li et al. 2006), which show the evolution of strain at the surface of the sandstone samples as a function of water content.

Figure 14 shows the cloud maps of the strain field at different time points for the corresponding number of cycles in dry, semi-saturated (water content 1.01%), and water-saturated sandstone samples under graded cyclic loading–unloading. According to Fig. 14a, after twenty cycles,
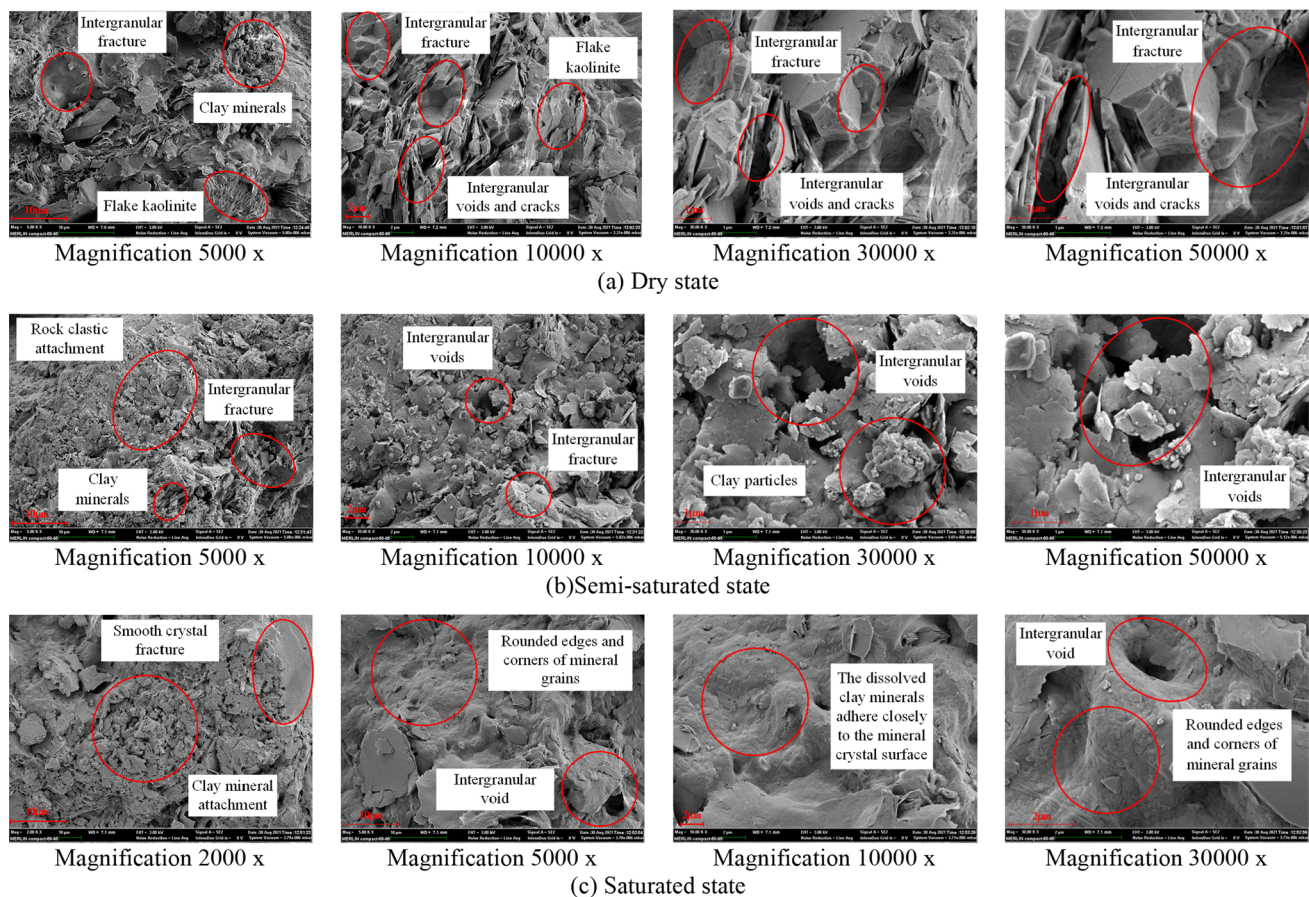

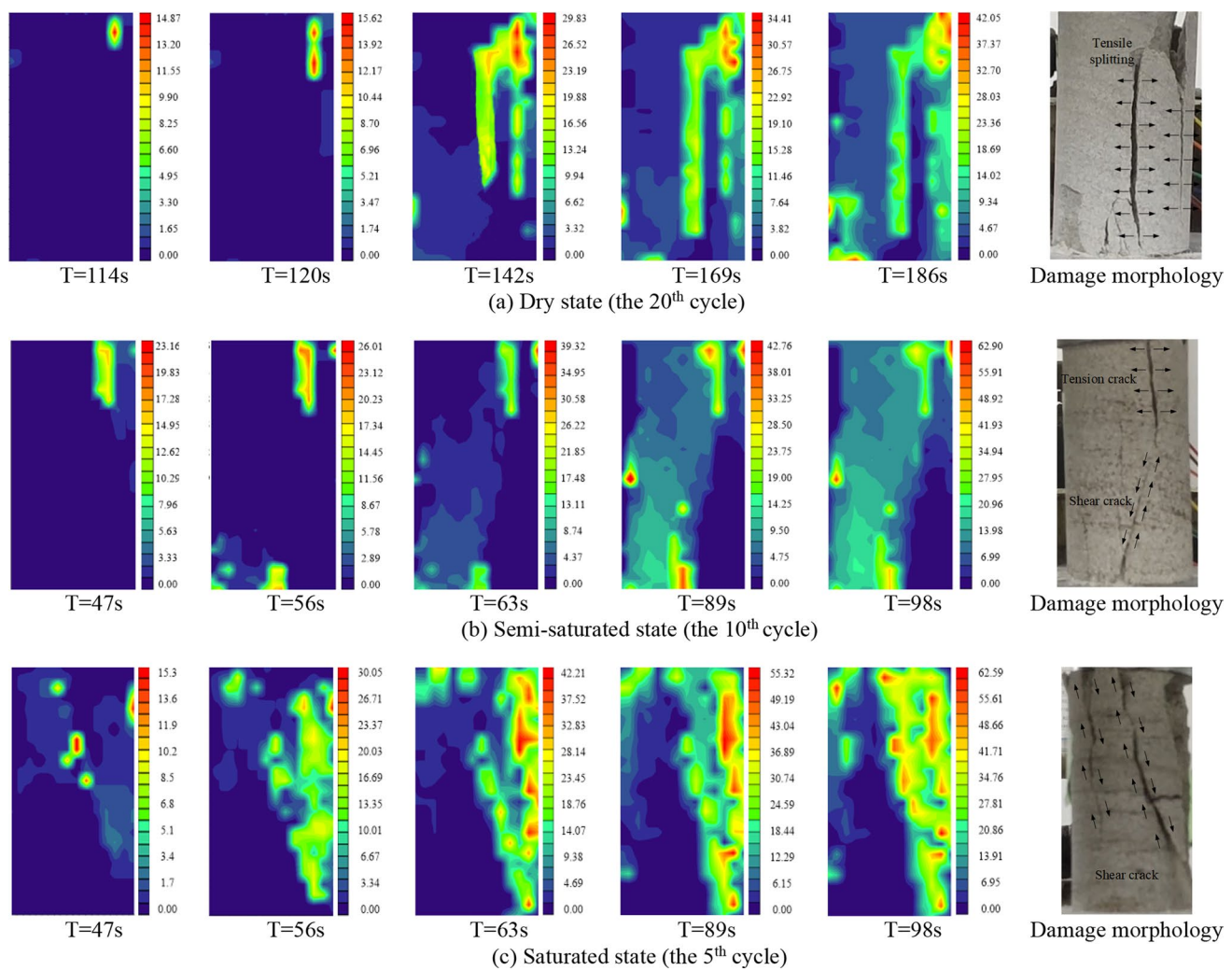**Fig.13** Micro-structural characteristics of sandstone samples

Fig. 14 Cloud maps of sandstone strain field with different water contents under graded cyclic loading–unloading conditions

cracks successively initiate from the upper and lower edges of the dry sandstone sample. Later, the cracks propagate in the principal stress direction and develop into three tensile cracks growing parallel to the loading direction. The sandstone sample then undergoes a splitting failure. According to Fig. 14b, cracks successively initiate from the upper-right and the lower-middle parts of the semi-saturated sandstone sample. The cracks first propagated along the loading direction and then merge into a single crack. The sandstone samples fail in tensile-shear mixed mode. According to Fig. 14c, cracks initiate from the middle of the saturated sandstone sample and gradually propagate. Inclined cracks are generated in the upper and lower parts of the sample. The sandstone sample has a single inclined-plane shear failure mode.

As the water content increases, the failure mode changes from tensile-brittle cleavage fracture in the dry state to tensile-shear mixed-mode failure. In the water-saturated state, sandstone samples undergo single shear failure with some ductile features. Meanwhile, more and more secondary fissures are generated near the main fracture, resulting in increasingly complicated patterns in the strain field cloud maps. The most probable explanation is that the sandstone bulk becomes damaged due to lubrication, wedging, and corrosion by water. As a result, a shear zone appears. In addition, as the water content increases, the shear zone within the sample became increasingly prominent. The presence of the shear zone contributes to the shear slip failure of the sandstone samples under stress.

7 Discussion

According to the above analyses, the mechanical properties of sandstone samples permanently deteriorates as the water content increases, whereas the damage accumulates gradually. Both the compressive strength and the energy-storage

characteristics deteriorate significantly. This phenomenon is primarily attributed to physical interactions between water and sandstone, which are briefly summarized below.

"Coal measures" is a lithostratigraphic term for the coal-bearing part of the upper carboniferous system, which consists of rocks such as claystone, shale, siltstone, and sandstone, interstratified with the beds of coal. Coal measures sandstone is a sedimentary rock composed of mineral particles of varying sizes and shapes. It has many bulk defects, including microcracks, fissures, and pores. In water-immersion tests, the water first rapidly fills the pores and fissures between the mineral particles. If the water immersion lasts for a long period, the pore water gradually permeates to the surface of the mineral particle to form bound water. Under the external force action, the sandstone samples undergo frictional slip between the mineral particles. As the amount of bound water increases on the mineral particle surfaces, its lubricating and softening effects are enhanced, which weakens the bonding between particles, decreasing the frictional coefficient and the cohesive force within the sandstone.

According to SEM and XRD analysis of typical fractures, the sandstone is mainly composed of quartz, feldspar, and clay minerals; on the microscopic scale, the fracture surface gradually rounds. The cracks and fissures within the sandstone samples are the primary sites where the physical and mechanical interactions occurred between water and rocks. As the water content increases, the calcareous cement is more likely to dissolve and corrode upon contact with water, and the soluble substances enter the immersion solution due to the movement of the water molecules. Therefore, the pores and fissures grow and become more rounded. In addition, the clay minerals expand due to water absorption with the water–rock interaction. Expansion stress then concentrates significantly at the crack tip, promoting crack initiation and propagation. The mineral particles on the surfaces of new cracks then undergo another round of physical reactions, including dissolution and expansion due to water absorption. These interactions promote the continuous damage and failure of sandstone. Under the joint action of these factors, the macro-mechanical parameters and the energy-storage characteristics of sandstone deteriorate as the water content increases.

The analysis of the test results reveals that the deterioration of the mechanical parameter and the failure modes of sandstone samples vary with water content, which implies that the physical impact of water on sandstone depends on the stage of water immersion. At the initial stage of water immersion, the water–rock interaction primarily features the absorption of water molecules by mineral particles. With the extension of soaking time, the water–rock interaction is dominated by the swelling purification of clay minerals, and the physical reaction is gradually enhanced. The secondary porosity increases within the sandstone samples under

physical action. The area of rock-water interaction increases, and the area and degree of bonding between mineral lparticles decreases. The mineral-particle skeleton is thus gradually weakened. The sandstone samples become looser and weaker in structure, the brittleness decreases, and the failure mode changes from brittle to ductile.

8 Conclusions

(1) The content and composition of rock-forming minerals in sandstone have no clear relationship with water content. However, with increasing water content, the uniaxial compressive strength, elastic modulus, and elastic storage limit of sandstone all gradually decrease, and the elastic strain of sandstone decreases under the same normalized cycle.

(2) Under graded cyclic loading and unloading, the input energy of sandstone is stored mostly in the form of elastic energy, whereas the dissipated energy is mostly in the form of work to overcome damping. The larger the water content of sandstone, the faster the growth of the damage factor, and the water accelerates the mechanical damage of sandstone. With increasing cycle number, the proportion of damping energy increases gradually first and then tends to stabilize. When the normalized cycle number approaches unity, the fraction of damping energy plummets, and that of the plastic energy increases sharply.

(3) With increasing water content, the effect of pore water on the lubrication, water wedge, and dissolution of mineral particles is enhanced, mineral particles are gradually rounded, and friction damping between particles is weakened, which makes the sandstone gradually evolve from a dense structure to a weak structure. More and more secondary fractures appear around the main fractures in sandstone, and the strain field becomes more and more complex. The failure mode of sandstone gradually changes from tension-splitting brittle failure to shear failure.

Availability of data and materials The datasets used and/or analyzed in the current study are available from the corresponding author upon reasonable request.

Declarations

References

Bian ZF, Zhou YJ, Zeng CL et al (2021) An discussion of the basic problems for the construction of underground pumped storage reservoir in abandoned coal mines. J China Coal Soc. https://doi.org/10.13225/j.cnki.jccs.YG21.0392

Chen GQ, Li TB, Wang W et al (2019) Weakening effects of the presence of water on the brittleness of hard sandstone. Bull Eng Geol Environ 78:1471–1483

Fan JY, Xie HP, Jie C et al (2020) Preliminary feasibility analysis of a hybrid pumped-hydro energy storage system using abandoned coal mine goafs. Appl Energy 258:114007

Geng JS, Cao LW (2020) Failure analysis of water-bearing sandstone using acoustic emission and energy dissipation. Eng Fract Mech 231:107021

Gu DZ (2015) Theory framework and technological system of coal mine underground reservoir. J China Coal Soc 40:239–246

Guo PY, Gu J, Su Y et al (2021) Effect of cyclic wetting–drying on tensile mechanical behavior and microstructure of clay-bearing sandstone. Int J Coal Sci Technol 8(5):956–968

Hashiba K, Fukui K (2015) Effect of water on the deformation and failure of rock in uniaxial tension. Rock Mech Rock Eng 48:1751–1761

Hua W, Li JX, Dong SM et al (2019) Experimental study on mixed mode fracture behavior of sandstone under water-rock interactions. Processes 7:70

Jardon S, Ordonez A, Alvarez R, Cienfuegos P et al (2013) Mine water for energy and water supply in the central coal basin of Asturias (Spain). Mine Water Environ 32(2):139–151

Kuwahara Y, Kyamamoto I, Hirasawa T (1990) An experimental and theoretical study of inelastic deformation of brittle rocks under cyclic uniaxial loading. Tohoku Geophys J 33(1):1–21

Li YH, Jing HW, Zeng QY (2006) Development and application of digital photographic measurement software system for geotechnical engineering. Chin J Rock Mech Eng S2:3859–3866

Li TB, Chen ZQ, Chen GQ et al (2015) An experimental study of energy mechanism of sandstone with different moisture contents. Rock and Soil Mech 36(S2):229–236

Li W, Wang DH, Li HJ (2019) Environmental engineering issues induced by abandoned coal mine hidden disasters. IOP Conf Ser Earth Environ Sci 237:022039

Liu Y, Dai F, Dong L, Xu NW (2018) Experimental investigation on the fatigue mechanical properties of intermittently jointed rock models under cyclic uniaxial compression with different loading parameters. Rock Mech Rock Eng 51(1):47–68

Ma CQ, Li HZ, Niu Y (2018) Experimental investigation on the mechanical behavior and damage evolution mechanism of water-immersed gypsum rock. Environ Earth Sci 77:23

Niu SJ, Ge SS, Yang DF et al (2018) Mechanical properties and energy mechanism of saturated sandstones. J Cent South Univ 25(6):1447–1463

Pu H, Bian ZF, Zhang JX et al (2021) Research on a reuse mode of geothermal resources in abandoned coal mines. J China Coal Soc 46(2):677–687

Stevens JL, Holcomb DJ (1980) A Theoretical investigation of the sliding crack model of dilatancy. J Geophys Res 85(B12):7091–7100

Sun K, Fan LM, Xia YC et al (2021) Impact of coal mining on groundwater of Luohe Formation in Binchang mining area. Int J Coal Sci Technol 8(1):88–102

Wang H, Yang TH, Liu HL et al (2017) Mechanical properties and energy evolution of dry and saturated sandstones under cyclic loading. Rock Soil Mech 38(6):1600–1608

Wong LNY, Maruvanchery V, Liu G (2016) Water effects on rock strength and stiffness degradation. Acta Geotech 11:713–737

Xie H, Ju Y, Li L (2005) Criteria for strength and structural failure of rocks based on energy dissipation and energy release principles. Chin J Rock Mech Eng 24:3003–3010

Xie H, Zhao JW, Zhou HW et al (2020) Secondary utilizations and perspectives of mined underground space. Tunn Undergr Space Technol 96:103129

Yu Y, Tang SB, Tang CA (2019) Experimental study on the influence of water content on instantaneous and creep mechanical properties of red sandstone. J China Coal Soc 44(2):473–481

Zhou ZL, Cai X, Cao WZ et al (2016) Influence of water content on mechanical properties of rock in both saturation and drying processes. Rock Mech Rock Eng 49:3009–3025